SI Appendix to accompany
Eocene greenhouse climate revealed by coupled clumped isotope-Mg/Ca thermometry

The raw data discussed in this manuscript can be found in Appendix Tab. A1a-d and A2a-b. Tab. A1 contains the raw Δ_{47} values (heated gas lines, modern and fossil sample data, and information necessary to transfer these raw data into the absolute reference frame). Tab. A2 contains the compilation of Eocene clumped isotope and Mg/Ca SST reconstructions shown in main text Fig. 3 and 4, including previously published planktonic Mg/Ca-derived SST revised using our $\mathrm{Mg/Ca_{sw}}$ curve.

Further clumped isotope details. Clumped isotope analysis is described in the Methods, and in detail elsewhere (1, 2). Following ref. (3), Δ_{47} is defined as:

$$\Delta_{47} = \left[\left(\frac{\mathrm{R}^{47}}{\mathrm{R}^{47*}} - 1\right) - \left(\frac{\mathrm{R}^{46}}{\mathrm{R}^{46*}} - 1\right) - \left(\frac{\mathrm{R}^{45}}{\mathrm{R}^{45*}} - 1\right)\right] \times 1000 \qquad \text{(eq. 1)}$$

Where, for example, R^{47} is the sample mass 47/44 ratio, and R^{47*} is that which would be expected if all ^{13}C and ^{18}O were distributed randomly among isotopologues.

We do not apply a pressure baseline correction (4) to our m/z 47 measurements because the typical Yale heated gas Δ_{47}-δ_{47} slope is relatively shallow (m_{HGL} = 0.003-0.006 over the analytical period of these samples). Furthermore, we observe no correlation between raw Δ_{47} and the pressure imbalance between the sample and reference bellows, which is a suggested test for whether a pressure baseline correction is necessary (5). Instead, we use the heated gas Δ_{47}-δ_{47} slope to correct sample measurements, i.e. $\Delta_{47}^{HG} = \Delta_{47}^{raw} - (\delta_{47}\times m_{HGL} + c_{HGL})$, where m_{HGL} and c_{HGL} are the slope and intercept of the heated gas line for a given analytical period. We then account for scale compression due to randomization in the ion source using the equation $\Delta_{47}^{streched} = \Delta_{47}^{HG}/(- c_{HGL} /0.87)$. See the supplementary information of ref. (1) for details.

To enable direct comparison with foraminifera samples measured in other laboratories and reported prior to the implementation of the absolute reference frame, all data (samples and standards) were first transferred into the 'Ghosh' reference frame as previously described (2, 3). Absolute Δ_{47} was then calculated using a transfer function based on analyses of heated gases, CO_2 equilibrated with H_2O at 25°C, Carrara Marble and cylinder CO_2. Tab. A1d gives two transformation equations using both the 'Gonfiantini' and 'Brand' parameter sets (see below), although we note that the choice of these parameters does not impact our palaeotemperature reconstructions because our LBF calibration is empirical (see below).

Twenty-one analyses of Carrara Marble over the same period as the samples yield mean Δ_{47} of 0.401±0.019‰, in agreement with a four-lab average of 0.395‰ (range 0.385-0.403‰) (6). In addition, frequent analyses of cylinder CO_2 were made, to ensure consistency with the previously reported value for the Yale laboratory (2). One standard was analyzed every day, of which more than half were heated gases over the entire analytical period.

Recently it has been suggested (7, 8) that the isotopic parameters used by most clumped isotope laboratories, including Caltech (3) and Yale, require revision. Specifically, the choice of parameters defining the abundance of ^{17}O and ^{13}C in SMOW and PDB exert a control on calculated Δ_{47}. We refer to the revised parameter sets as 'Brand' for those advocated by ref. (7) and 'Gonfiantini' for those formerly used in most laboratories. Δ_{47} values calculated using both parameter sets are shown in Tab. S2 and S4. In each case the heated gases and other laboratory standards used for transforming data into the absolute reference frame were reprocessed using the same parameter set as the data. For samples and standards with δ^{13}C and δ^{18}O close to that of the reference gas, such as the foraminifera analyzed here, the choice of parameters exerts only a small control on Δ_{47}. Specifically, the absolute Δ_{47} measurements shift by -0.009‰ on average when switching from the Gonfiantini to Brand parameter sets. Consequently, this is not a significant source of uncertainty in our data. However, recalculating the Yale inorganic calibration line (9) using the Brand parameter set results in a +0.021‰ shift in the intercept (the change in slope is not significant), because these inorganically precipitated carbonates are characterized by δ^{13}C between -30‰ and -35‰, much lower than the reference gas. Although each data set should be recalculated individually, similar shifts are expected in many calibrations that are based on inorganic precipitation, in which low δ^{13}C values are typical (10). Therefore, the inorganic calibration line is inconsistent with Δ_{47} values in modern biogenic carbonates measured at Yale, and cannot be used to estimate temperature in absolute Δ_{47} space using the Brand parameters. We circumvent these issues by using our modern LBF data to define the intercept of a biogenic calibration line. Specifically, we fit a linear regression through the modern sample data using the slope of inorganic carbonates analyzed in the Yale laboratory (9), as recalculated using the Brand parameters (Fig. S1). This inorganic slope is used as the modern LBF do not cover a large enough temperature range to precisely define a biogenic slope. The resulting Yale foraminifera calibration in the absolute reference frame is:

$$\Delta_{47} = 0.0537 \cdot \frac{10^6}{T^2} + 0.092 \qquad \text{(eq. 2)}$$

Whilst this foraminifera calibration line may not be suitable for use with samples measured in other laboratories, it ensures that our paleotemperatures will not require revision as advances are made in carbonate clumped isotope calibrations and inter-laboratory calibrations.

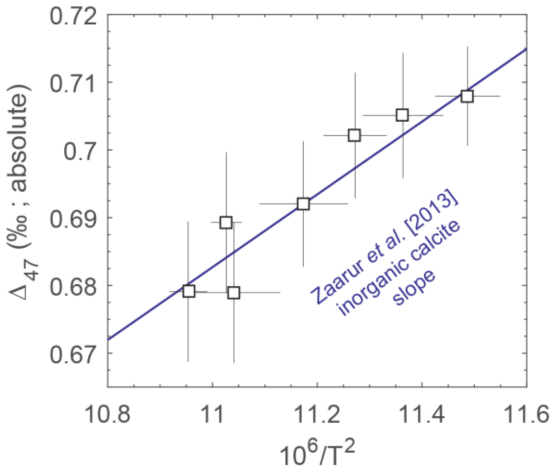

Fig S1. Δ_{47} analyses of live-collected LBF (Tab. S1) and calibration based on these data and the inorganic calcite slope (9), see text for details.

Foraminifera clumped isotope details.

Sample errors were calculated based on the standard deviation of 21 Carrara Marble measurements described above (0.019‰), performed over the same analytical period as the samples. Foraminifera samples were analyzed in 3-9 replicates resulting in 1SE precision calculated using the reproducibility of Carrara Marble of 0.007-0.012‰. For comparison, 1SE sample precision ranges between 0.005-0.024‰, and only one sample is characterized by worse precision than Carrara Marble (pooled standard deviation 0.017‰, i.e. 0.002‰ better than the standard). This is likely the result of minor heterogeneities in the Carrara Marble standard.

Previous modern foraminifera Δ_{47} analyses are given in refs. (11, 12). There is insufficient information reported to reprocess these data into the absolute reference frame using the different parameter sets described above. Therefore, we compare our modern foraminifera data to these studies using the 'Ghosh' reference frame (13), as it is this in which previous data were reported (Fig. S2). Because the analytical reference gas composition used in all these studies is similar in composition to CO_2 derived from typical marine carbonates, any shift as a result of the choice of the parameter sets described above will be small, and similar between laboratories. Consequently, any relative difference between our dataset and these previous studies will be similar in any reference frame. Importantly, we observe no significant offset between our LBF data and low-Mg calcite foraminifera (Fig. S2).

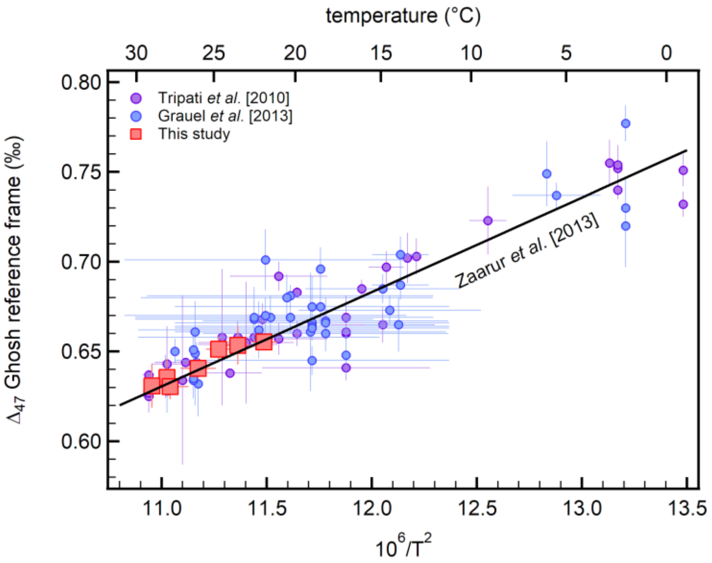

Fig S2. Δ_{47}-temperature calibration in live-collected LBF compared to core-top foraminifera. Data are shown in the Ghosh reference frame as the accurate conversion of previous foraminifera clumped isotope data into the absolute reference frame is not possible based on published data. All calcification temperatures are from the World Ocean Atlas, errors are the seasonal range. Δ_{47} uncertainties are 1SE.

The necessity of sample cleaning prior to Δ_{47} analysis as described above was investigated using three modern and fossil samples (Fig. S3). These samples were initially crushed and analyzed with no pretreatment, then cleaned and analyzed again, see Methods and Fig. S3 caption for cleaning procedure details. With the exception of one Fossil sample (KW03, see Tab. S4), the difference between Δ_{47} measured on these cleaned versus uncleaned powders is within analytical uncertainty. Based on these data we cannot demonstrate that cleaning is necessary on either live-collected or fossil material, although we routinely applied these procedures as clay contamination and/or organic material is likely to be sample-specific and may be important in certain cases. Importantly, the cleaning procedure we apply is sufficiently mild to avoid affecting Δ_{47} values of samples without remnant organics.

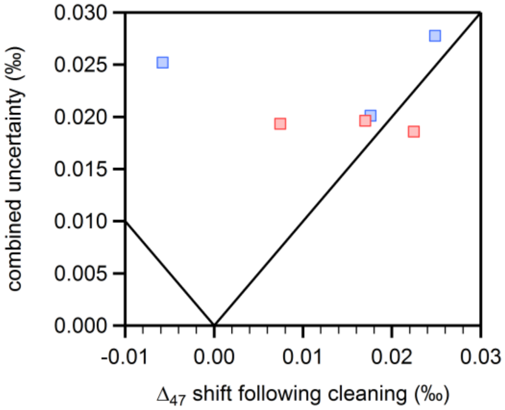

Fig S3. The effect of cleaning procedures applied to modern and fossil LBF (blue and red squares respectively) on Δ_{47}. Modern samples were ultrasonicated in H_2O_2 and H_2O; methanol and H_2O was used for fossil material. A positive shift in Δ_{47} denotes higher values following cleaning. With the exception of one fossil sample, the Δ_{47} shift following cleaning is smaller than the combined error (1SE), depicted by the diagonal black lines.

Sample preservation. Exceptional preservation of fossil foraminifera was assessed in two ways, SEM imaging and spatially-resolved laser-ablation analysis (see Methods). SEM images of modern and Eocene specimens are shown in Fig. S4. Comparing a live-collected modern specimen to the Eocene material (Fig. S4, panels A and B) demonstrates that there is no infilling of the pores and no evidence of $CaCO_3$ overgrowths. The broken chamber walls are characterised by the same texture, indicating that fine-scale recrystallisation has not taken place. Laterally-broken specimens (i.e. split along the marginal chord, see (14)), show no chamber infilling or evidence of overgrowths, have open pores, and fine-scale features such as the spiral canal system are preserved (note the structures running parralel to the marginal chord highlighted with arrows in Fig. S4C,F).

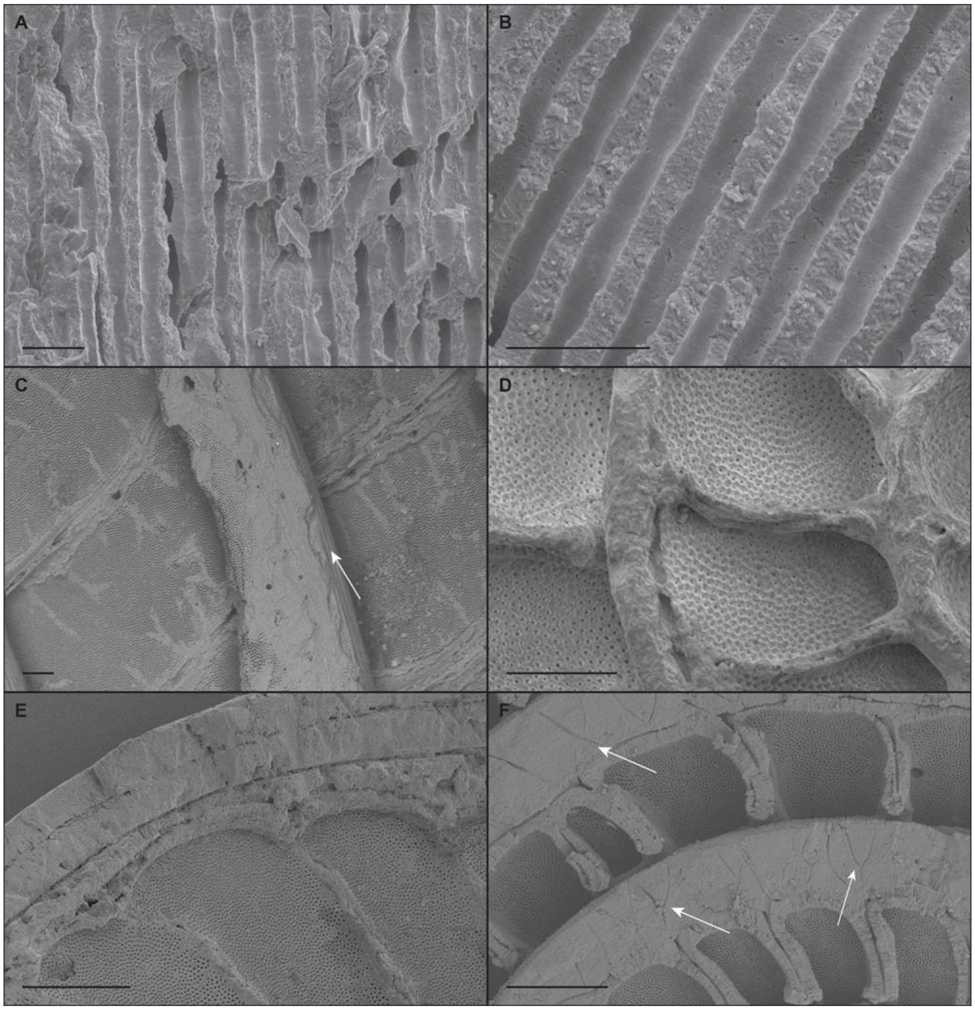

Fig. S4. SEM images of modern (A) and fossil (B-F) nummulitid foraminifera. (A) Broken chamber wall of a live-collected *Operculina ammonoides* from sample SS07613 (Tab. S1). (B) Comparative broken chamber wall of an Eocene *Nummulites djokdjokartae* specimen from sample KW03. (C) Laterally broken section showing the marginal chord and chamber wall surface of a specimen from sample W10-3c. (D) Lateral broken section of K136.4, (E) Section of Ke57.5, and (F) Section of EF1 showing open pores and marginal chord structures (white arrows). Scale bars 10 µm (panels A,B), 100 µm (panels C,E,F), 40 µm (panel D). Arrows point to regions in which fine scale structures (the spiral canal system) are visible within the marginal chord.

As described in the Methods, the excellent visual preservation was also confirmed geochemically by laser-ablation ICPMS trace element analyses of the majority of the specimens analysed for clumped isotopes. All individual LA-ICPMS analyses, including multiple replicates on indiviudal specimens (summarised in Tab. S3), are displayed in Fig. S5. One advantage of utilising the nummulitid foraminifera is that their shell is composed of high-Mg calcite. Upon diagenetic recrystallisation it undergoes rapid conversion to low-Mg, low-Sr calcite. As such, there is no continuum in Mg/Ca-Sr/Ca space between well-preserved and poorly-preserved samples (Fig. S5), which means that Mg/Ca and Sr/Ca ratios can be used to unambiguously identify recrystallised samples. We do not report clumped isotope temperatures for any poorly-preserved samples, so to illustrate this point three visually-recrystallised samples not discussed in the main text are shown in Fig. S5 (FL1 from the Hampshire Basin, UK, and further samples from Oman (15) and Adelholzen, S. Germany (16)). These are clearly distinct from visually well-preserved specimens, and would yield impossible (negative) calcification temperatures based on Mg/Ca <30 mmol mol^{-1}.

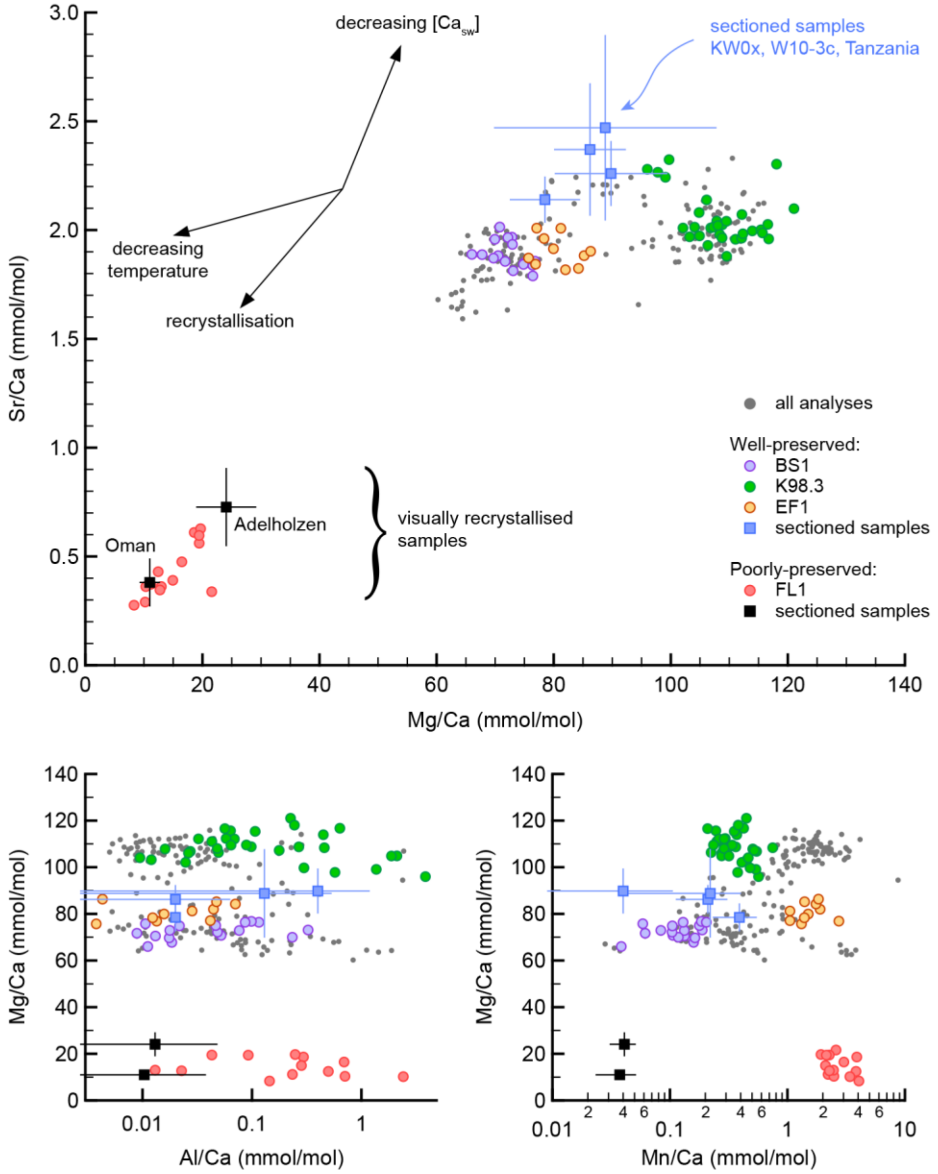

Fig. S5. Trace element data for all specimens/samples on which clumped isotope measurements were made. (A) Mg/Ca-Sr/Ca. All data are shown (grey dots) with selected samples highlighted to demonstrate no correlation within a group of specimens, which could indicate simulatenous diagenetic loss of Mg and Sr. Note the lack of continuum between the well-preserved material presented here (high Mg and Sr) and examples of visually recrystallised specimens (Oman, Adelholzen, FL1). Black data points with 2SD uncertainties represent samples that were analysed by placing a laser track around the marginal chord of multiple sectioned specimens (see (19)). Those with multiple data points represent samples that were repeatedly non-destructively analysed (by depth profiling into the marginal chord of multiple whole specimens). The approximate trajectories of different processes impacting Mg and Sr incorporation are shown for reference. (B) Mg/Ca-Al/Ca, showing no evidence for a clay contaminant phase with sufficient Mg to affect our calcite Mg/Ca measurements. (C) Mg/Ca-Mn/Ca, similarly showing no evidence for high Mg-Mn overgrowths.

Whilst this enables recrystallisation to be geochemically assessed, we also measure Al/Ca and Mn/Ca ratios as indicators of possible clay contamination and high Mn-Mg overgrowths, following previous studies (17, 18). We observe no correlation between Mg/Ca and either Al or Mn for any sample (Fig. S5), in line with visual observations (Fig. S4) suggesting that observable overgrowths are not present.

The application of LBF to SST and Mg/Ca$_{sw}$ reconstruction. The shallow-dwelling large benthic foraminifera that we utilize have a peak depth-abundance distribution within the top 50 m of the ocean throughout southeast Asia (20) and within the top 20 m in many locations globally (e.g. ref (21)). This is approximately equivalent to the depth of planktonic foraminifera usually considered to be surface-dwelling, such as *Globigerinoides ruber* (found at ~20 m in the Red Sea (22)) and *Trilobatus sacculifer* which has been estimated to calcify between 0-50 m in the North Atlantic (23). Based on the 2013 World Ocean Atlas (24), 90% of the ocean at 30 m depth is within 1°C of SST and 80% at 50 m is within 2°C of SST (Fig. S4). Therefore, whilst all 'surface-dwelling' foraminifera may underestimate true SST by up to 1°C, reconstructions based on these LBF are as representative of SST as planktonic species. Because the habitat depth of these foraminifera is frequently characterized by an *in-situ* temperature equivalent to that of SST we do not apply a depth correction as (1) in many cases this would lead to an overestimate, and (2) this facilitates direct comparison to previous studies utilizing foraminifera geochemical data. We note that *Operculina ammonoides* has photosymbionts, and carbon isotope data of fossil *Nummulites* (described in ref. (25)) demonstrates that this was likely also the case in the equivalent Eocene foraminifera. Hence, nummulitids cannot live outside the photic zone. Furthermore, the merit of the coupled Δ_{47}-Mg/Ca data is the constraint that these provide on Mg/Ca$_{sw}$, which is invariant throughout the ocean, even in coastal sites. This is because riverine water contains far less Mg and Ca than seawater (~110× and ~12× less respectively (26)), so that a very large reduction in seawater salinity by riverine freshwater is required before the Mg/Ca$_{sw}$ ratio can be altered significantly. Specifically, a 3% bias in Mg/Ca$_{sw}$ would require a ~10 psu salinity reduction, and a 10% bias requires a salinity approximately half that of open ocean (Fig. S7). A salinity reduction of this magntiude is highly unlikely in sediments containing marine fauna. In the mid-high latitude continental shelves $\delta^{18}O_{sw}$ may be influenced by freshwater, as a small salinity reduction may shift the seawater isotopic composition by several permil, yet even away from the tropics this cannot be large enough to affect Mg/Ca$_{sw}$. This is supported by our mid-latitude $\delta^{18}O_{sw}$ reconstructions which are no more than 2-3‰ more negative than the bulk Eocene ocean. Therefore, whilst our LBF are unavoidably from shelf sites, the majority of the data in our SST compilation (Fig. 4) cannot be biased by the location of our samples, given that our Mg/Ca$_{sw}$ reconstruction (and therefore our planktonic Mg/Ca reanalysis) is not sensitive to the proximal location of our LBF sample sites.

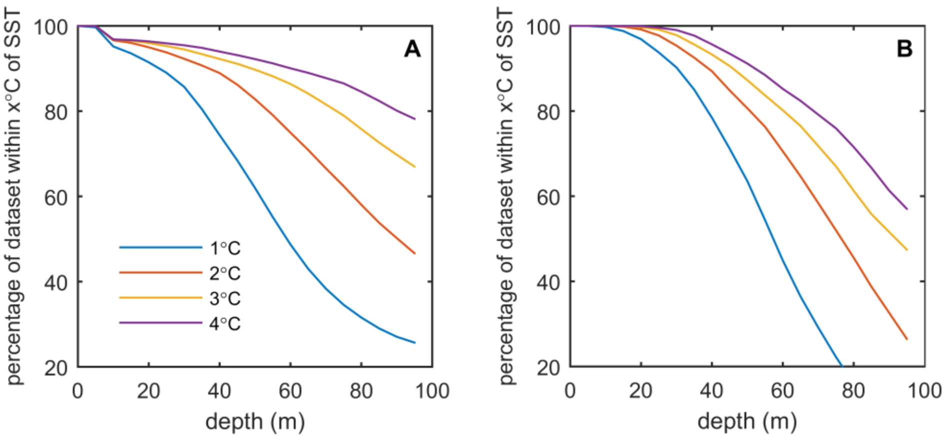

Fig S6. The offset between the temperature of the surface ocean and depths of 5-95 m, as a percentage of all measurements in the 2013 World Ocean Atlas (24). (A) The global ocean, (B) The tropics. For example, at 30 m depth 90% of the ocean is within 1°C of SST based on this dataset. The peak abundance of nummulitid foraminifera in southeast Asia is 20-30 m (20).

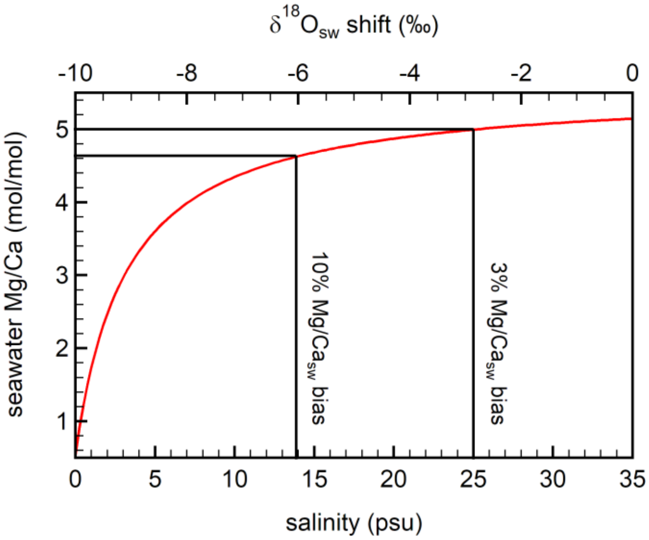

Fig S7. The relationship between seawater salinity and Mg/Ca$_{sw}$ (assuming deviation from 35 psu is due to riverine input), based on the average global riverine [Mg] and [Ca] of ref. (26) and seawater Mg/Ca = 5.2 mol mol^{-1} (53/10.3 mM). The salinity reduction required to bias Mg/Ca$_{sw}$ by 3% and 10% are indicated. $\delta^{18}O_{sw}$ scales linearly with salinity at a given site and time interval. One possible example is shown for the case of $\delta^{18}O_{freshwater}$ 10‰ more negative than seawater.

Fossil sample site palaeogeography. For detailed sample site information see references in Tab. S4. Nanggulan (Java) was situated on the southern edge of the SE Asian shelf (27), with *Nummulites* present in fine/medium-grained sand beds in the middle Eocene. There is no sedimentological or fossil evidence for a restricted environment at the time. Kutch was located on the northwest Indian shelf (28). Strontium isotopes of equivalent *Nummulites* to those utilized here show no evidence for freshwater input (29). The palaeogeography of Tanzania is discussed in detail elsewhere (30, 31). Briefly, the drill sites are estimated to be approximately 50 km from the palaeo-shoreline, distal of a narrow shelf (31). The sedimentary facies and smaller benthic foraminiferal biofacies suggest that the sediment was deposited in a bathyal outer shelf to slope setting, at ~300-500 m water depth. The larger foraminifera have been penecontemporaneously redeposited from the shelf setting (see (30) for details), where they occur alongside corals, echinoids, bryozoans, molluscs and dasyclads; all typical of shallow tropical platform environments. The open-ocean nature of these tropical shelf sites is also borne out by our $\delta^{18}O_{sw}$ data, which are within error of calculated mean ocean water in an ice-free world (see main text and Tab. S4), with the exception of the latest-Eocene *Nummulites* from Tanzania. Samples from northwest Europe come from the Hampshire (UK), Belgium and Paris basins. The palaeogeography of this region is variable through the Eocene (32) due to local or global sea-level change (33). LBF are found in offshore silty clays and sands, although we note that $\delta^{18}O_{sw}$ data from these samples potentially indicate a degree of freshwater input to these sample sites. Nonetheless, the calculated $\delta^{18}O_{sw}$ values (Tab. S4), at most 3‰ below mean Eocene seawater, do not represent a salinity reduction large enough to bias our Mg/Ca_{sw} reconstructions (Fig. S7).

Early Eocene climatic change in northwest Europe. As described in the main text, we analyze samples from the Southern UK (Hampshire Basin), Paris Basin and Belgium Basin (Tab. S3), principally to fill gaps in our Mg/Ca_{sw} reconstruction. Nonetheless, these data also represent the first Δ_{47} record of early-mid Eocene climatic change in northwest Europe. These clumped isotope results are shown in Fig. S8 in the context of two mid/high-latitude TEX_{86} records, from the Southern Ocean (34) and West Siberian Sea (35), ~65°S and 55°N respectively. All three datasets are characterized by warming of 7-9°C between the earliest Eocene and the EECO. Our Δ_{47} data confirm that this previously identified (36) long-term warming was also a feature of northwest Europe, and demonstrate excellent agreement between Δ_{47} and TEX_{86}^{H} (at least to the extent that comparing globally-distributed sites is a good test of inter-proxy agreement). Similarly, the long-term cooling evident in the ODP Site 1172 TEX_{86} data and the benthic oxygen isotope stack (34, 37) is also manifest in our northwest European Δ_{47} measurements, which delineate 7°C SST cooling between the EECO and mid-Eocene.

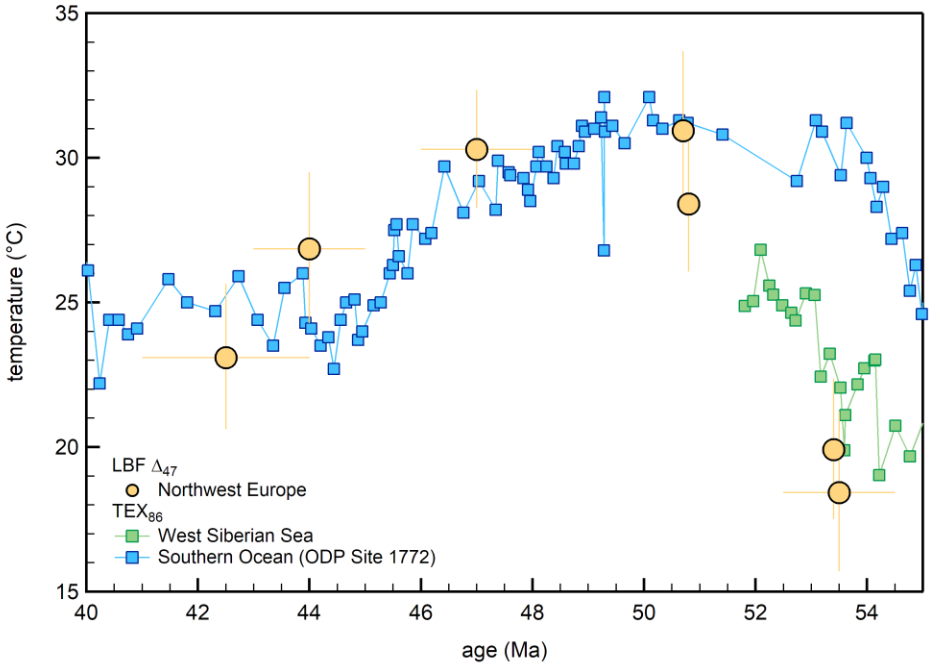

Fig. S8. Comparison of our northwest European LBF clumped isotope temperatures to previously published mid/high-latitude TEX_{86}^{H} (34, 35).

Seawater Mg/Ca reconstruction. We reconstruct seawater Mg/Ca (Mg/Ca_{sw}) by measuring both temperature (clumped isotopes) and shell Mg/Ca of the same Eocene LBF sample. These data, along with the present-day Mg/Ca_{sw} ratio, can then be used to solve the coupled Mg/Ca_{test}-temperature-Mg/Ca_{sw} calibrations for this group of foraminifera (38) which takes the following form:

$$\mathrm{Mg/Ca_{LBF}} = \frac{-1.98 \cdot (\mathrm{Mg/Ca}_{\mathrm{sw}}^{\mathrm{t=t}})^2 + 37.0 \cdot \mathrm{Mg/Ca}_{\mathrm{sw}}^{\mathrm{t=t}}}{-1.98 \cdot (\mathrm{Mg/Ca}_{\mathrm{sw}}^{\mathrm{t=0}})^2 + 37.0 \cdot \mathrm{Mg/Ca}_{\mathrm{sw}}^{\mathrm{t=0}}} \cdot 91.8\ exp^{0.0183T} \qquad \text{(eq. 3)}$$

Where Mg/Ca_{LBF} is the measured shell Mg/Ca, $Mg/Ca_{sw}^{t=t}$ is the Eocene Mg/Ca_{sw} ratio to be reconstructed, $Mg/Ca_{sw}^{t=0}$ is the present-day Mg/Ca_{sw} ratio (~5.2 mol mol^{-1}), T is temperature in Celsius, and the constants are empirically defined, see ref. (39) for a detailed explanation. Uncertainty in the Δ_{47} temperature and laser-ablation ICPMS Mg/Ca measurement are propagated to Mg/Ca_{sw}. The mean combined uncertainty on Mg/Ca_{sw} is 0.25 mol mol^{-1} which is derived approximately equally from these two sources. Mg/Ca_{sw} reconstruction with an uncertainty of this magnitude represents a ~2-5 times improvement over other techniques, such as ridge flank calcium carbonate veins (CCVs) (40, 41), fluid inclusions in halite (42), coral (43), and echinoderm calcite (44), see Fig. 2 and S9. We also note that some sources of uncertainty in previous reconstructions were not propagated into Mg/Ca_{sw}, implying that the uncertainty on previously reported values may have been underestimated. For example, the relationship between seawater and shell Mg/Ca is not well constrained for corals or echinoderms (unlike these LBF), and there is uncertainty with respect to which Mg distribution coefficient (D_{Mg}) should be applied to ridge vein carbonates (41).

We recalculate the ridge calcium carbonate vein Mg/Ca data as the original reconstructions assume a linear relationship between calcite and seawater Mg/Ca (41), whereas inorganic laboratory precipitates demonstrate that this relationship is quadratic over the range that $\mathrm{Mg/Ca_{sw}}$ has varied over the Phanerozoic (45, 46):

$$\mathrm{Mg/Ca_{calcite}} = -1.96 \cdot \mathrm{Mg/Ca_{sw}}^2 + 26.9 \cdot \mathrm{Mg/Ca_{sw}} \quad \text{(eq. 4)}$$

In practice this has a small effect on the ridge vein carbonate data, although it has the effect of reducing the offset between these and our reconstructions to <0.1 mol $\mathrm{mol^{-1}}$ over the period that reconstructions based on CCV and LBF overlap (30-40 Ma; Fig. 2). The agreement between these proxies throughout this interval is better than the uncertainty on either, indicating that they are likely to be both precise and accurate. Furthermore, the coherency of our reconstructions between seven globally-distributed sites provides strong evidence that spatially-variable oceanographic parameters (e.g. salinity, $[\mathrm{CO_3^{2-}}]$) do not exert a resolvable control on nummulitid Mg/Ca or Δ_{47}. This is in contrast to low-Mg planktonic species, but in agreement with data from live-collected LBF field specimens (19) and culture data of *Operculina* (47), the nearest living relative of the Eocene *Nummulites*. The lack of significant secondary influences on Mg incorporation in nummulitid calcite is probably because these foraminifera lack a mechanism of reducing the Mg/Ca ratio of the calcifying fluid (38); a process that leads to such complications in low-Mg species (48). Deriving absolute temperatures from planktonic foraminifera Mg/Ca in the Paleogene with a precision useful for model-data comparison are possible only in the context of our precise and continuous $\mathrm{Mg/Ca_{sw}}$ record.

In order to produce the composite Paleogene seawater Mg/Ca record shown in Fig. 2 (see Tab. S5), we utilize both our LBF and the recalculated CCV data (41) (as described above). Using a bootstrap approach, 1000 resampled datasets were created by adding a random error to both the age and $\mathrm{Mg/Ca_{sw}}$ values for each reconstruction, within the range of the maximum uncertainty for each data point. Each of these was LOESS smoothed (robust, quadratic, smoothing 0.35) and re-sampled at 0.1 Ma resolution in order to avoid loss of structure in these LOESS curves before production of the final curve. Reconstructed $\mathrm{Mg/Ca_{sw}}$ with 95% confidence intervals is based on the 5th, 50th and 95th percentile of this dataset, down-sampled to 1 Ma to reflect the average resolution of the original data (20 reconstructions over the period 30-55 Ma). It should be noted that the downward $\mathrm{Mg/Ca_{sw}}$ trend between 34-30 Ma is a largely driven by one LBF and one CCV-derived reconstruction at 31 and 30 Ma respectively, which may require future revision. This is similarly the case in the earliest Eocene, characterized by a decreasing trend between 56-54 Ma driven by one LBF data point. The $\mathrm{Mg/Ca_{sw}}$ curve is within error of no change over these intervals and, although our composite curve substantially reduced the uncertainty in Eocene-Oligocene $\mathrm{Mg/Ca_{sw}}$, caution should be exercised in the interpretation of fine-scale changes.

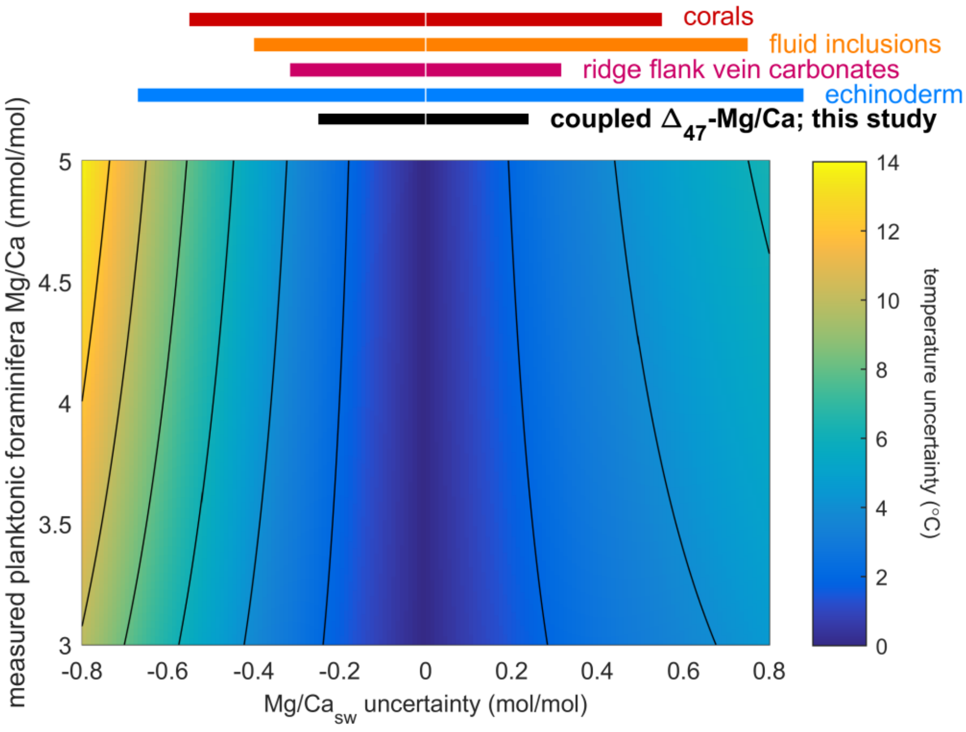

Fig S9. The uncertainty on planktonic foraminifera Mg/Ca-derived palaeotemperatures resulting from the uncertainty on Mg/Ca$_{sw}$ (depicted by color; contours are shown at 2°C intervals). Horizontal colored bars at the top of the graph relate to the same x-axis and show the typical magnitude of errors of proxy Mg/Ca$_{sw}$ reconstructions. Those from this study are 2-5× smaller than most previous techniques, reducing the error in absolute planktonic Mg/Ca temperatures to <2-3°C.

Comments on seawater Mg/Ca. There are few previous Paleogene Mg/Ca$_{sw}$ reconstructions with which to compare our data. Coral Mg/Ca has been used to examine the evolution of seawater Mg/Ca (43), however these data are associated with errors of ±50%; as evident in the range of Eocene-Oligocene reconstructions from 1.75-4.25 mol mol^{-1}. One data point at ~53 Ma derived from echinoderm Mg/Ca (44) is in good agreement with our reconstruction. This lack of data has meant that many previous studies reporting temperature based on Mg/Ca have had no choice but to use the output of coarse-resolution models of Mg/Ca$_{sw}$ (49, 50), although they were not designed for this purpose. Neither of these models agree with our reconstruction, with the implication that previous work may have significantly under or overestimated paleotemperature depending on which model was used.

We conservatively calculate the maximum latitudinal SST gradient by comparing our tropical SST data to deep water temperatures derived from benthic foraminifera Mg/Ca, therefore secular changes in seawater chemistry need to be taken into account when interpreting these data. We utilize the Mg/Ca compilation of ref. (51), which itself uses the Mg/Ca$_{sw}$ record of ref. (52), a coarse-resolution model based on a Ca isotope record and parameterization of other processes controlling the Mg and Ca cycle (e.g. sea-floor spreading rate is related to the seawater Sr isotope record). This model is not widely used for calculating foraminifera Mg/Ca temperatures, however the application of this reconstruction to the benthic foraminifera data is fortuitous because this model is in good agreement with our proxy reconstructions in the Eocene (the two are within 10%). Therefore, we do not update the deep water temperatures of ref. (51) because a 10% difference in Mg/Ca_{sw} exerts a negligible impact on these temperature reconstructions. Note that the benthic foraminifera dataset is unique in this respect, the Mg/Ca_{sw} record of ref. (52) has not been applied to any planktonic foraminifera data and therefore these require revision as detailed above.

On the thermal tolerance of foraminifera. Both planktonic and benthic foraminifera are characterized by high mortality rates when exposed to temperatures of 33-34°C in laboratory cultures (53, 54). However, the response of these organisms to near-instantaneous warming is unlikely to represent their ability to adapt over thousands or millions of years – the timescales relevant to Eocene warming. Moreover, some LBF have been observed living in the thermal plume of a power station at up to 42°C (55, 56), indicating that certain foraminifera may adapt to extreme warmth relatively quickly. Both planktonic and large shallow benthic foraminifera are abundant throughout the Eocene tropics, which is unlikely to have been the case if these organisms were poorly adapted to the conditions at the time. Aside from the sample sites reported here, which include locations within a few degrees of the equator, it has been shown that an increase in diversity of shallow LBF coincided with the PETM at another subtropical site (Egypt; ref. 57). Lastly, seasonal cycles have been observed in the geochemistry of shallow-dwelling large benthic foraminifera from one of our tropical sites (19), indicating that they calcify continuously throughout the year. Together, these observations provide strong evidence that foraminifera were not only able to tolerate, but were well adapted to the tropical conditions during the early Eocene.

Planktonic foraminifera Mg/Ca reanalysis. All published planktonic foraminifera Mg/Ca data were reinterpreted based on recent advances in our understanding of the control that pH and Mg/Ca_{sw} exert on Mg incorporation in these organisms, as well as utilizing the new Paleogene Mg/Ca_{sw} curve described above (see Tab. A2 for the data compilation). In order to account for the influence of pH on shell Mg/Ca, we use a modelled Cenozoic pH record (58). The purpose of this seawater pH reconstruction was to examine geological-scale shifts in seawater carbonate chemistry and therefore lacks the fine detail of likely pH variation (59), especially in response to climatic events associated with a carbon cycle perturbation. Therefore, we add a ±0.2 pH unit uncertainty propagated through to the corrected planktonic foraminifera Mg/Ca data, which is the maximum offset between the Cenozoic model and boron isotope reconstructions (59, 60). In order to convert measured planktonic foraminifera Mg/Ca into temperature, we first correct the raw ratios for the difference between in seawater pH between the modern and Paleogene using the Mg/Ca-pH relationship of ref. (48):

$$\mathrm{Mg/Ca_{norm}} = \frac{\mathrm{Mg/Ca_{measured}}}{\frac{0.66}{1+\exp(6.9\cdot(\mathrm{pH}-8.0))}+0.76} \qquad \text{(eq. 5)}$$

Note that the available laboratory culture data indicate that this correction is independent of Mg/Ca_{sw}. pH-normalized Mg/Ca is then converted to temperature using the Mg/Ca-temperature equations of ref. (22), which also consider the response of planktonic foraminiferal Mg/Ca to Mg/Ca_{sw}. These maintain an exponential relationship of the form $Mg/Ca_{foraminifera} = B\exp^{AT}$, where:

$$B = 0.019\cdot \mathrm{Mg/Ca_{sw}}^2 - 0.16\cdot \mathrm{Mg/Ca_{sw}} + 0.804 \qquad \text{(eq. 6)}$$

$$A = -0.0029\cdot \mathrm{Mg/Ca_{sw}}^2 + 0.032\cdot \mathrm{Mg/Ca_{sw}} \qquad \text{(eq. 7)}$$

A dissolution correction was not applied to the data because the possible spatial variation in these parameters is not well-constrained in the Eocene. Similarly, the uncertainty resulting from salinity was not propagated through to Mg/Ca-derived temperatures because the salinity influence is relatively minor (a 2-3 psu salinity change translates to a 1°C temperature bias (61)), and the mean Eocene ocean was within 1 psu of modern (62). The error in Paleogene Mg/Ca-derived temperatures resulting from a ±0.2 pH unit uncertainty and ~0.2 mol mol^{-1} Mg/Ca_{sw} precision are temporally variable because shell Mg/Ca depends nonlinearly on both parameters (Fig. S10). Broadly, the SST error is smaller when pH is lower (as Mg/Ca is insensitive to pH below ~7.8 (48)) and Mg/Ca_{sw} is higher. Mean Paleogene absolute Mg/Ca-derived temperature uncertainty originating from pH and Mg/Ca_{sw} is 4.7°C, but is lower during the early Eocene (~3-4°C over the interval 55-48 Ma) than the late Eocene and Oligocene (~6°C).

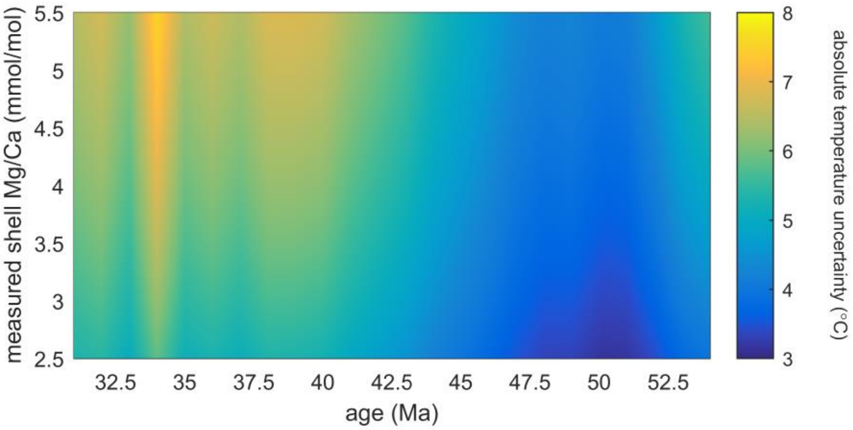

Fig S10. The error in Paleogene planktonic foraminifera Mg/Ca-derived temperatures as a result of a 0.2 unit uncertainty in pH (based on the Cenozoic pH record of ref. (58)) and Mg/Ca_{sw} uncertainty from Fig. 2.

Our Mg/Ca reanalysis is dependent on the Mg/Ca_{sw} reconstruction shown in Fig. 2 and therefore on our Δ_{47} values. It therefore provides a non-circular test of our palaeotemperatures. For example, if we were to reconstruct higher Δ_{47} temperatures, our LBF-derived Mg/Ca_{sw} record would shift to lower values and absolute planktonic foraminifera Mg/Ca-derived SST would rise as a higher component of shell Mg/Ca would result from temperature. Therefore, it is important to note that the observed agreement between our clumped isotope and reevaluated planktonic foraminifera Mg/Ca temperatures (Fig. 3,4) is not the result of the dependency of our planktonic Mg/Ca-derived temperatures on our Mg/Ca_{sw} record. This is because the relationship between Δ_{47}-derived temperature, our Mg/Ca_{sw} reconstruction and the subsequent reanalysis of Mg/Ca temperatures is nonlinear. If we were to reconstruct higher Δ_{47} temperatures, our planktonic Mg/Ca SST would also be higher, but the two proxies would no longer be in agreement. For example, a 5°C higher or lower clumped isotope temperature would shift the two proxies out of agreement in the tropics by ~3-4°C. The inter-proxy agreement in the Eocene tropics is not coincidental but a direct outcome of precise Δ_{47}-derived Mg/Ca_{sw} reconstructions which enables us to accurately correct Mg/Ca data for the first time.

GDGT data treatment. Recalculation and compilation of GDGT values into temperature using the $\text{TEX}_{86}^{\text{H}}$ (GDGT-2) calibration was mostly based on previous compilations of these data (36, 63). It is beyond the scope of this study to address GDGT calibration issues. We utilize the

TEX_{86}^{H} calibration globally in order to avoid qualitatively biasing the dataset by choosing different calibrations for different sites and time intervals, but note that the TEX_{86}^{L} calibration (64) and interpretation of GDGT in terms of subsurface temperatures in the Eocene (65) may result in a more favorable model-data comparison at high latitudes.

Calculating model and data mean latitudinal gradients. The latitudinal gradients shown in Fig. 5 were necessarily calculated in different ways given the differing resolution of each dataset.

Modern: The mean modern latitudinal SST gradient is calculated using the 1° resolution 2013 World Ocean Atlas dataset (24). It is defined here as the difference between the mean of all tropical and high latitude (<23° and >58°) temperatures at 0 m depth, and is equal to 26.0°C.

Data: The average early Eocene proxy gradient was calculated by comparing the mean of all available tropical SST data (i.e. the early Eocene portion of the compilation shown in Fig. 4) to the mean of the benthic foraminifera Mg/Ca-derived deep ocean temperature record (51) for the interval 55.5-48 Ma (no PETM samples were included). The uncertainty is derived from the maximum range given by adding or subtracting 2SE to both the tropical SST and deep-ocean Mg/Ca temperature record (as we are interested in constraining the average gradient). As discussed in the main text, our analysis may represent a best-case scenario with respect to model-data comparison, as it is possible that deep water formation occurred predominantly in winter or in the cooler/more saline parts of the high latitude oceans (if this is the case then our gradient is steeper than the globally-averaged mean annual). Deep-ocean benthic foraminifera Mg/Ca was used as a proxy for high latitude SST because high-latitude SST reconstructions may be warm-season biased (66), and it has been noted that early-mid Eocene benthic foraminifera $\delta^{18}O$ and Mg/Ca data are substantially lower than the coolest high latitude SST (67), although this is not the case for some Δ_{47} data from long-lived organisms (68), see Fig. 3. Significant cooling of high latitude-sourced surface water during subduction to the deep ocean is not possible, although some areas of the Eocene oceans may have been more stratified than at present. This may particularly be the case in the Arctic where there is evidence that salinity was significantly lower than the other ocean basins during some parts of the Eocene (69). For these reasons, we emphasize that latitudinal SST gradients calculated in this way may reflect maximum steepness endmembers.

Using the modern ocean as a test of this method, the mean deep ocean (>2000 m) is 1.7°C and the high latitude surface ocean (>58°N/S) is -0.3°C (24) (both numbers are the annual median). The deep ocean is warmer on average than the high-latitude surface ocean, reflecting the fact that much of the high-latitude surface ocean is colder than the regions of deep water formation, which is density driven. Nonetheless, the offset between these two datasets is smaller than the uncertainty in any paleotemperature reconstruction. Therefore, utilizing the average deep ocean as a proxy for high-latitude SST may counteract the complications we describe above. Whilst there is evidence for reorganization of ocean circulation during at least some parts of the Eocene (70, 71), the locations of deep water formation are poorly constrained. We assume that the broad similarity of globally averaged deep ocean and high latitude SST holds irrespective of the dominant locations of deep water formation.

Even in light of our data the Eocene ocean is overall poorly spatially sampled. For example, there are no data points from the West Pacific or Indian Ocean for the late Eocene, and the overall lack of tropical SST for the mid-Eocene (38-48 Ma) means that performing a similar exercise for this interval could result in a bias towards mean SST gradient that is too low because the available data are dominated by a clumped isotope measurement from within an expanded West Pacific Warm Pool. However, early Eocene SST reconstructions are based on clumped isotopes, Mg/Ca and TEX_{86} from five sites, and the gradient from this interval is well-constrained.

Model: Eocene model SST gradients were calculated in the same way as the modern ocean, by comparing the mean of all tropical versus high latitude SST grid squares, except that Eocene gradients were normalized to the respective pre-industrial control simulation rather than the present-day latitudinal gradient. The only exception to this was the CCSM model of ref. (72), as the pre-industrial simulation is characterized by a high-latitude cool bias. Instead, the pre-industrial gradient was calculated using the high latitude SST from an alternative CCSM pre-industrial simulation (73).

Location-specific model-data comparison. Previously published Eocene proxy data is from refs. (17, 34, 35, 48, 67, 68, 74–91). Mg/Ca and clumped isotope data is compiled in Tab. A2a-b.

In order to directly compare model simulations and proxy data (Fig. 5B), Eocene proxy data were binned into three time intervals (34-38, 38-48 and 48-56 Ma), following previous studies that use similar bins (34, 92). The latter interval broadly represents peak Eocene warmth to which models are frequently compared, although it was a time of significant transient and long-term climatic change (17, 34, 51). Splitting the early Eocene into narrower time windows does not impact our main conclusions (see main text), and we do not do so because the sparsity of data risks introducing regional bias into the analysis.

Binned proxy data were then compared to the respective model grid cells (Fig. S12-14). Model SST was calculated based on the nearest model grid cell and those surrounding it (i.e. open ocean proxy data were compared to the mean of nine model cells), in order to avoid bias from artifacts within any single model cell. The high latitude comparisons (i.e. the boxes shown in Fig. S12-14) were defined by comparing the median model high latitude SST to the mean of the deep-ocean Mg/Ca data for the same intervals. Doing so assumes that the bottom water temperature record represents a globally averaged signal that approximates SST in the high latitudes, and therefore requires no knowledge of deep water circulation or formation (see above).

Sample site paleolatitude is based on the paleomagnetism reference frame, following ref. (93). An unavoidable complication is that model paleogeography differs from that of the paleomagnetism reference frame. We do not analyse the proxy data in the same (hotspot) reference frame as the models, because this reference frame places some key southern hemisphere high-latitude sites at paleolatitudes that are too far south (93). The compromise employed here is to compare proxy data in the paleomagnetic reference frame to the same palaeolatitude in the models even though plate positions between the model and proxy data reference frames are consequently not the same.

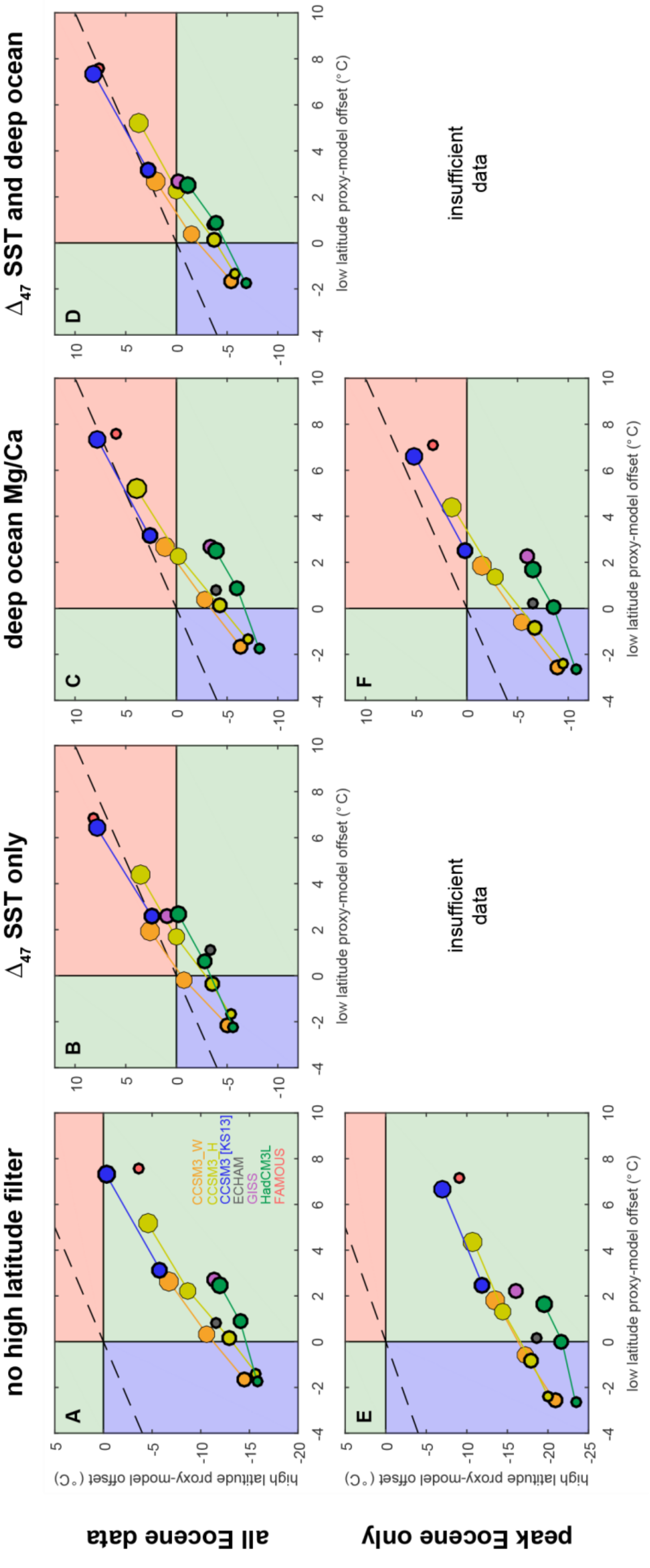
no high latitude filter
Δ47 SST only
deep ocean Mg/Ca
Δ47 SST and deep ocean
A
B
C
D
E
F
all Eocene data
peak Eocene only
CCSM3_W
CCSM3_H
CCSM3 [KS13]
ECHAM
GISS
HadCM3L
FAMOUS
insufficient data
insufficient data
high latitude proxy-model offset (° C)
low latitude proxy-model offset (° C)
-4
-2
0
2
4
6
8
10
5
0
-5
-10
-15
-20
-25
10

Fig S11. Sensitivity of model-data comparison to chosen Eocene datasets. (A) All Eocene proxy data. (B) All proxy data in low latitudes but only clumped isotope data at high latitudes. (C) All proxy data in low latitudes but high latitude SST calculated assuming that it is approximately equivalent to deep ocean temperature, as reconstructed by Mg/Ca in deep benthic foraminifera. (D) All proxy data in low latitudes and both clumped isotope and deep ocean Mg/Ca data combined to calculate high latitude SST. (E-F) show the same analysis including only peak Eocene data (48-56 Ma. Panel F is that shown in Fig. 5B in the main text. Two panels are missing because there are no published peak Eocene high-latitude clumped isotope data. Marker size shows model CO_2 (see Fig. 5 for concentrations); those with bold edges have CO_2 within the range of proxy data.

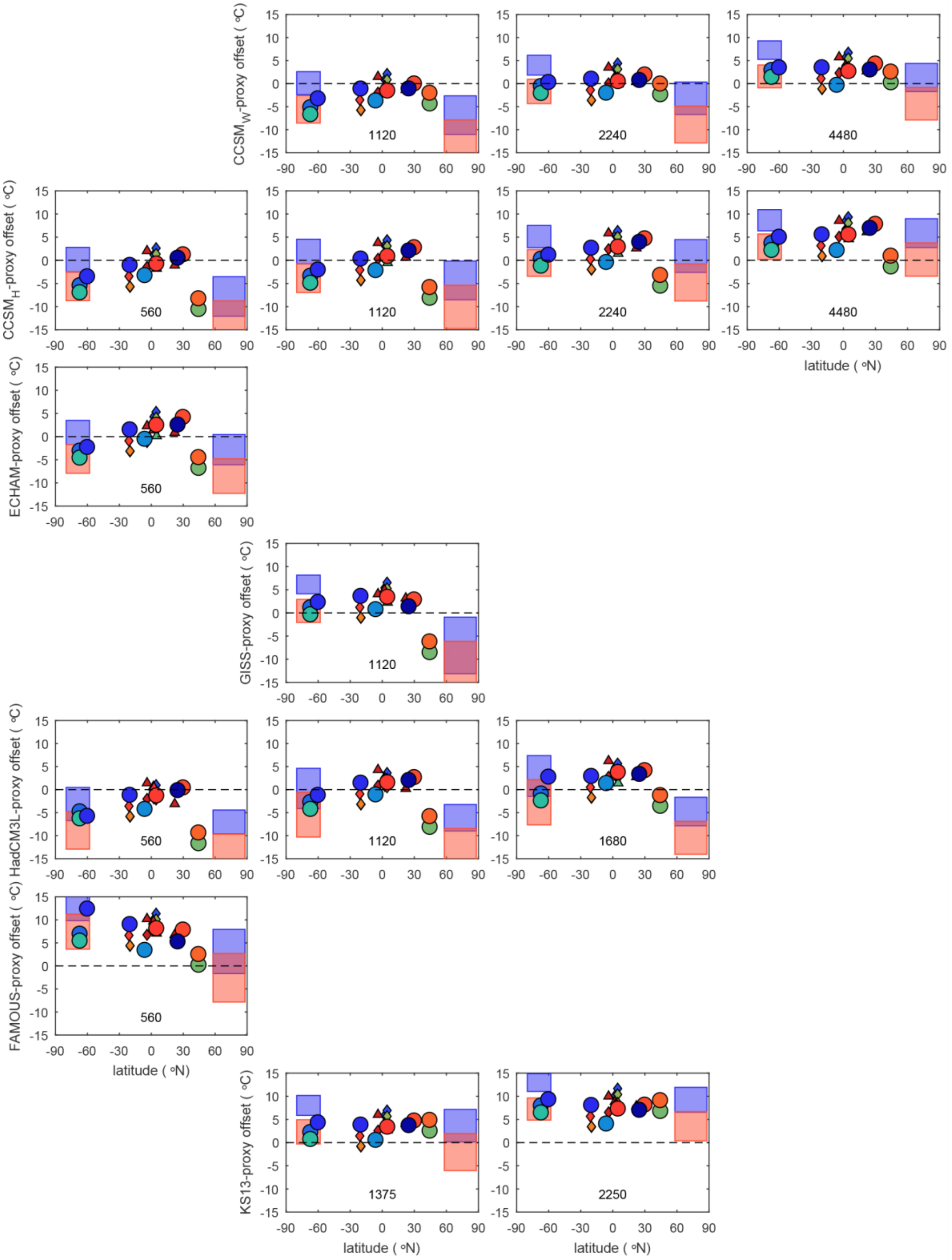

Fig S12. Location-specific proxy-model comparison. Where many datapoints are available for a given site and time interval these were binned into three time intervals, colour is shown as the mean age for a given site and time bin (see main text). Only Δ_{47} and deep ocean Mg/Ca (as a proxy for high latitude SST) are shown outside of the tropics (each plot is one datapoint in Fig. S11, panel D). See main text Fig. 5 for legend and color scale. The number at the bottom of each panel gives the CO_2 concentration (ppmv) used in each model run.

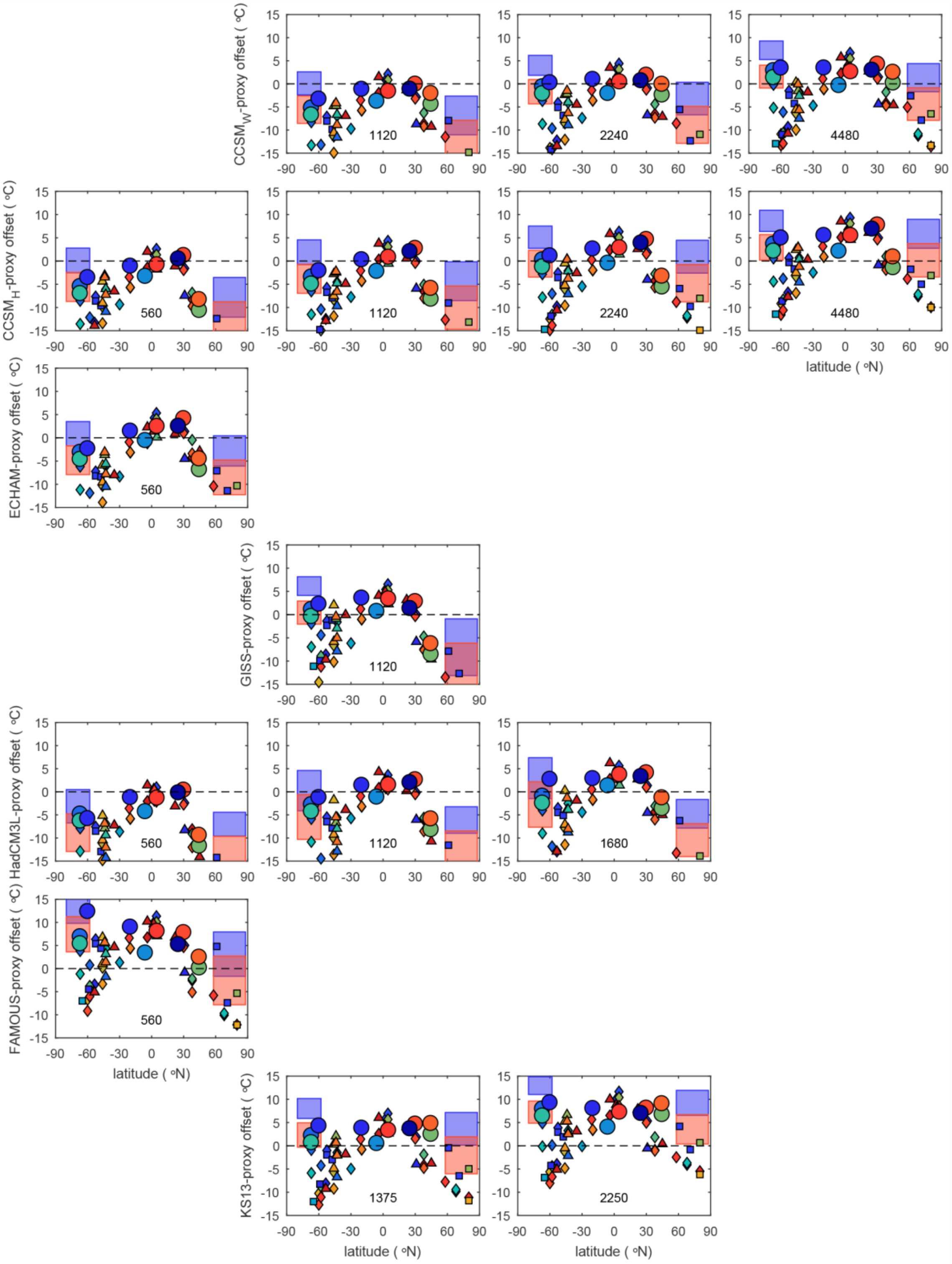

Fig S13. Location-specific proxy-model comparison using all proxy data (each plot is one datapoint in Fig. S11, panel A), binned into three time intervals.

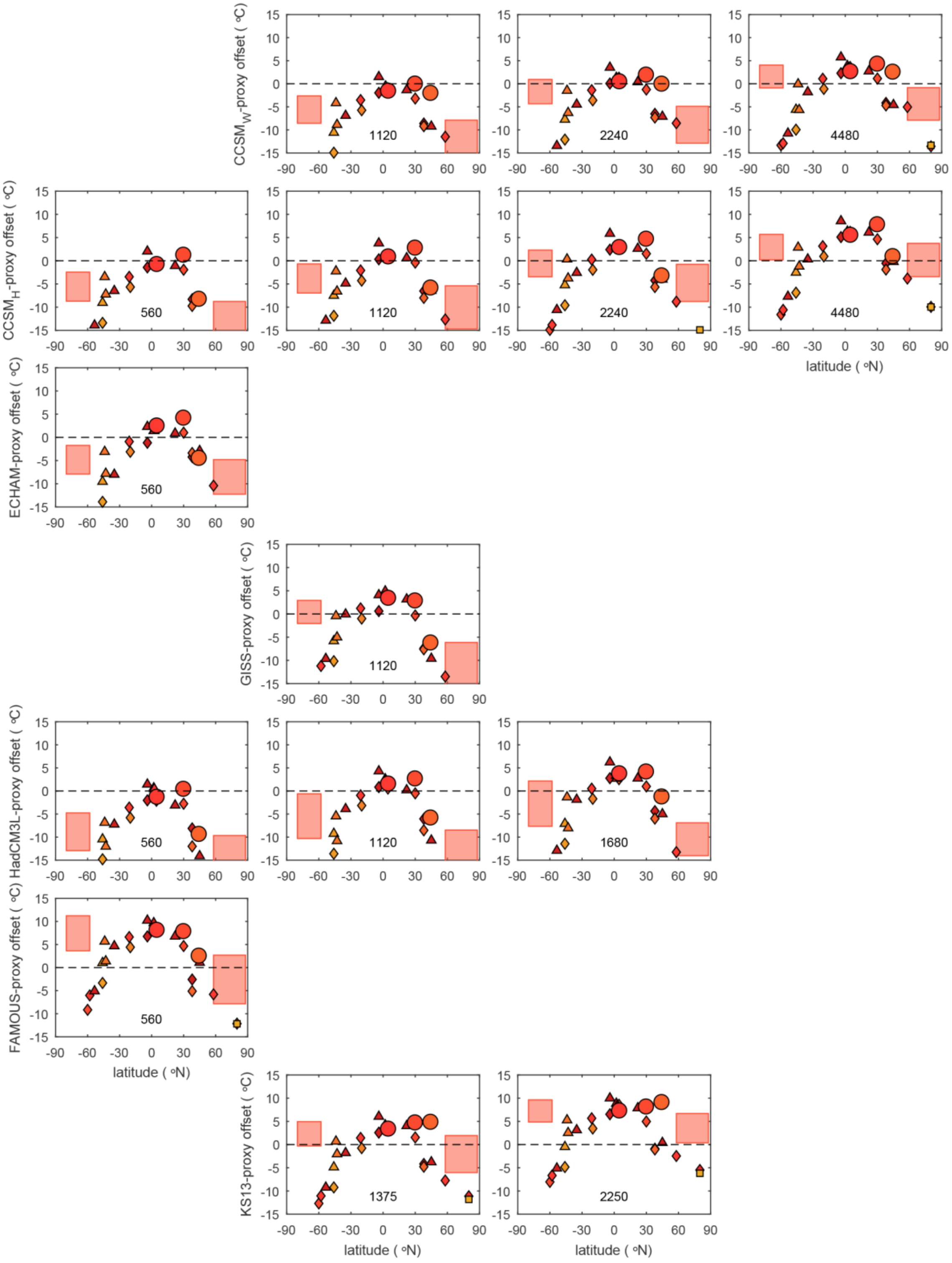

Fig S14. Location-specific proxy-model comparison for the early Eocene (48-56 Ma, each plot is one data point in Fig. S11, panel E).

Tab. S1. Clumped isotope data of live-collected LBF. Δ_{47} is given in the 'Ghosh' and the absolute reference frames, the latter using the isotopic parameter sets of both Gonfiantini and Brand, see SI text and ref. (7) for rationale and details. Further sample site details are given in ref. (19) and references therein.

sample	species[†]	location	MAT[‡] (°C)	seasonal 2SD (°C)	Δ_{47} (Ghosh)	Δ_{47} (Abs.; Gonfiantini)	Δ_{47} (Abs.; Brand)	n[*]	1SE	$\delta^{13}C_{cc}$ (‰ VPDB)	$\delta^{18}O_{cc}$ (‰ VPDB)
Eil12	*O. ammonoides*	Red Sea	21.9	0.8	0.655	0.716	0.708	8	0.007	0.13	0.63
Eil13	*O. ammonoides*	Red Sea	23.5	1.0	0.653	0.714	0.705	5	0.009	0.74	0.17
KKE30	*O. ammonoides*	SW Sulawesi	28.0	0.4	0.636	0.695	0.689	4	0.010	1.17	-2.47
SS07613	*O. ammonoides*	Great Barrier Reef	24.7	0.8	0.651	0.711	0.702	5	0.009	-1.00	-1.83
pd31	*H. depressa*	SW Sulawesi	26.0	1.1	0.641	0.700	0.692	5	0.009	1.07	-2.31
SER0	*O. ammonoides*	NW Java	29.0	0.5	0.631	0.690	0.679	4	0.010	-0.98	-2.84
CYCLO	*C. compressa*	Pedro Bank, Caribbean	27.8	1.2	0.631	0.690	0.679	4	0.010	3.97	-1.22

[†] *Operculina ammonoides* and *Heterostegina depressa* are nummulitid foraminifera, *Cyclorbiculina compressa* is a miliolid.

[‡] Sample site mean annual temperatures are taken from the World Ocean Atlas (24), except for the Red Sea for which nearby monitoring data are available.

[*] The number of analyses (n) refers to the number of replicate measurements of each sample.

Tab S2. Details of Paleogene sites shown in Fig. 1.

Sample	Location	Formation	Age (Ma)	Uncertainty	Paleolatitude	Species	Refs.[1]
BF8d	Mississippi, USA	Byram	31.0	1.0	25°N	Radiate *Nummulites*	(94)
17/36/2 80-95	Tanzania Drilling Project	Pande	33.9	0.0	20°S	Reticulate *Nummulites*	(30)
KW01	Nanggulan, Java	Nanggulan	39.0	1.0	6°S	*Nummulites djokdjokartae*	(19)
KW03	Nanggulan, Java	Nanggulan	39.0	1.0	6°S	*Nummulites djokdjokartae*	
SW1	Hampshire Basin, UK	Selsey	42.5	1.5	45°N	*Palaeonummulites* aff. *prestwichianus*	(32)
BS1	Balegem Sandpit, Belgium	Lede	44.0	1.0	45°N	*Nummulites aquitanicus*	
W10-3c	Isle of Wight, UK	Earnley	47.0	1.0	44°N	*Nummulites britannicus*	
K98.3	Kutch, India	Naredi	49.9	1.5	5°N	*Nummulites burdigalensis cantabricus*	(29, 95)
EF1	Ampe Quarry, Belgium	Hyon	50.7	0.1	45°N	*Palaeonummulites planulatus*	
EF2	Ampe Quarry, Belgium	Hyon	50.8	0.1	45°N	*Palaeonummulites planulatus*	
KE57.5	GSB Kester Borehole, Belgium	Mons-en-Pévèle	53.4	0.1	45°N	*Palaeonummulites planulatus*	
CJTT	Paris Basin, France	Cuise	53.5	1.0	43°N	*Palaeonummulites planulatus*	
K136.4	Kutch, India	Naredi	54.9	1.5	5°N	*Nummulites burdigalensis kuepperi*	
K/N-06/5	Kutch, India	Naredi	55.3	1.5	5°N	*Nummulites globulus nanus*	

[1] Where further details in the references pertain to all samples from a given location, they are shown only next to the youngest sample.

Tab S3. Laser-ablation ICPMS trace element data of fossil samples. Both the number of individual specimens analyzed (n(ind)) and the total number of analyses (n(anal)) are given, 3-5 laser spots were placed on each specimen to gain a representative mean. Most specimens were analyzed non-destructively by drilling into the marginal cord (38). In a few cases foraminifera were sectioned and a continuous laser path placed across the marginal chord (those labelled ‘ws’), enabling true mean values to be calculated for each specimen.

			mean ratios (mmol/mol)				2SE					
Sample	Age (Ma)	Unc.	Mg/Ca	Al/Ca	Mn/Ca	Sr/Ca	Mg/Ca	Al/Ca	Mn/Ca	Sr/Ca	n (ind)	n (anal)
BF8d	31.0	1.0	82.5	0.09	0.32	2.01	1.6	0.09	0.06	0.02	7	29
17/36/2 80-95	33.9	0.0	89.8	0.40	0.04	2.26	9.6	0.79	0.07	0.15	1	4
KW01	39.0	1.0	86.2	0.02	0.21	2.37	2.3	0.02	0.04	0.12	7	ws
KW03	39.0	1.0	88.8	0.13	0.22	2.47	8.5	0.18	0.08	0.19	5	ws
SW1	42.5	1.5	72.5	0.10	0.29	1.98	1.1	0.06	0.07	0.02	8	29
BS1	44.0	1.0	71.5	0.06	0.11	1.92	1.7	0.04	0.03	0.03	5	20
W10-3c	47.0	1.0	78.5	0.02	0.39	2.14	3.5	-	0.09	0.06	3	ws
K98.3	49.9	1.5	93.6	0.42	0.39	2.09	2.0	0.29	0.05	0.04	8	31
EF1	50.7	0.1	78.6	0.02	1.42	1.96	3.3	0.01	0.35	0.06	4	12
EF2	50.8	0.1	80.8	0.02	0.84	1.99	3.3	0.01	0.13	0.05	4	12
KE57.5	53.4	0.1	63.4	0.30	2.82	1.66	1.8	0.30	0.42	0.07	6	15
CJTT	53.5	1.0	68.2	0.21	0.40	1.76	1.8	0.16	0.05	0.04	4	16
K136.4	54.9	1.5	94.7	0.30	2.34	2.07	1.5	0.26	0.55	0.04	8	28
K/N-06/5	55.3	1.5	104.0	0.02	1.77	2.11	1.1	0.00	0.13	0.05	8	30
										Total:	78	226

Tab S4. Clumped isotope analyses of exceptionally-well preserved Paleogene large benthic foraminifera. Δ_{47} data are given in the 'Ghosh' (13) and absolute (6) reference frames, the latter based both on the isotopic parameter sets originally used by most laboratories (denoted 'Gonfiantini') and those advocated by ref. (7), denoted 'Brand'. Temperature is calculated from Δ_{47} in the absolute reference frame calculated using the 'Brand' parameter set, see text for details. Seawater Mg/Ca (Mg/Ca$_{sw}$) is calculated using these temperatures and the shell Mg/Ca data from Tab. S2, see text for details. $\delta^{18}O_{sw}$ was calculated using the foraminifera laboratory calibration of ref. (96).

Sample	Age (Ma)	±	Δ_{47} (Ghosh; Gonfiantini)	Δ_{47} (Abs.; Gonfiantini)	Δ_{47} (Abs; Brand)	1SE	n	Temp. (°C)	+	-	Mg/Ca$_{sw}$ (mol/mol)	+	-	$\delta^{13}C_{cc}$ (‰ VPDB)	$\delta^{18}O_{cc}$ (‰ VPDB)	$\delta^{18}O_{sw}$ (‰)
BF8d	31.0	1.0	0.637	0.696	0.679	0.012	3	29.4	3.1	3.0	2.24	0.25	0.23	1.18	-0.77	1.90
17/36/2 80-95	33.9	0.0	0.624	0.682	0.678	0.012	3	29.7	3.2	3.1	2.45	0.57	0.47	2.23	-2.89	-0.16
KW01	39.0	1.0	0.612	0.670	0.658	0.007	8	35.0	2.0	2.0	2.09	0.18	0.17	1.20	-4.79	-0.93
KW03	39.0	1.0	0.608	0.666	0.653	0.007	9	36.3	1.9	1.9	2.11	0.36	0.32	1.28	-4.79	-0.66
SW1	42.5	1.5	0.651	0.711	0.704	0.010	4	23.2	2.6	2.5	2.20	0.19	0.18	2.92	-5.47	-4.14
BS1	44.0	1.0	0.636	0.695	0.689	0.010	4	27.0	2.7	2.6	2.00	0.20	0.18	2.11	-2.48	-0.33
W10-3c	47.0	1.0	0.629	0.687	0.675	0.008	7	30.4	2.1	2.0	2.07	0.23	0.21	1.93	-4.68	-1.80
K98.3	49.9	1.5	0.611	0.669	0.657	0.009	5	35.1	2.6	2.5	2.29	0.22	0.21	0.99	-4.52	-0.64
EF2	50.7	0.1	0.627	0.686	0.673	0.010	4	31.1	2.8	2.7	2.11	0.26	0.24	2.30	-4.51	-1.49
EF1	50.8	0.1	0.640	0.700	0.682	0.009	5	28.5	2.4	2.3	2.16	0.25	0.23	1.98	-4.97	-2.49
KE57.5	53.4	0.1	0.665	0.726	0.717	0.010	4	20.0	2.5	2.4	2.01	0.20	0.18	-0.79	-3.31	-2.67
CJTT	53.5	1.0	0.671	0.732	0.724	0.012	3	18.5	2.8	2.7	2.26	0.24	0.22	1.17	-4.45	-4.13
K136.4	54.9	1.5	0.616	0.674	0.665	0.009	5	33.1	2.5	2.5	2.43	0.22	0.20	0.39	-4.56	-1.10
K/N-06/5	55.3	1.5	0.620	0.678	0.675	0.009	5	30.4	2.5	2.4	2.88	0.24	0.23	0.70	-4.56	-1.66

Tab. S5. Composite Paleogene seawater Mg/Ca reconstruction based on LBF and CCV data. The curve shown in Fig. 2 is the 50th percentile of 1000 LOESS bootstrap fits through the data accounting for the uncertainty on each individual data point.

age (Ma)	95% CI	50th percentile	95% CI
30	1.92	2.15	2.44
31	2.04	2.26	2.49
32	2.12	2.35	2.63
33	2.15	2.41	2.67
34	2.12	2.41	2.78
35	2.12	2.38	2.66
36	2.10	2.33	2.62
37	2.05	2.27	2.53
38	1.96	2.19	2.46
39	1.85	2.13	2.39
40	1.71	2.09	2.34
41	1.77	2.08	2.31
42	1.81	2.08	2.30
43	1.84	2.08	2.29
44	1.85	2.08	2.27
45	1.89	2.09	2.27
46	1.92	2.10	2.27
47	1.93	2.12	2.28
48	1.95	2.14	2.30
49	1.97	2.16	2.34
50	1.98	2.18	2.36
51	1.98	2.21	2.40
52	1.99	2.23	2.46
53	1.94	2.27	2.56
54	2.03	2.37	2.72
55	2.09	2.50	2.82

1. Zaarur S, Affek HP, Stein M (2016) Last glacial-Holocene temperatures and hydrology of the Sea of Galilee and Hula Valley from clumped isotopes in Melanopsis shells. *Geochim Cosmochim Acta* 179:142–155.
2. Affek HP (2013) Clumped isotopic equilibrium and the rate of isotope exchange between CO_2 and water. *Am J Sci* 313(4):309–325.
3. Huntington KW, et al. (2009) Methods and limitations of “clumped” CO_2 isotope (Δ_{47}) analysis by gas-source isotope ratio mass spectrometry. *J Mass Spectrom* 44:1318–1329.
4. He B, Olack GA, Colman AS (2012) Pressure baseline correction and high-precision CO_2 clumped-isotope (Δ_{47}) measurements in bellows and micro-volume modes. *Rapid Commun Mass Spectrom* 26(24):2837–2853.
5. Fiebig J, et al. (2016) Slight pressure imbalances can affect accuracy and precision of dual inlet-based clumped isotope analysis. *Isotopes Environ Health Stud* 52(1–2):12–28.
6. Dennis KJ, Affek HP, Passey BH, Schrag DP, Eiler JM (2011) Defining an absolute reference frame for “clumped” isotope studies of CO_2. *Geochim Cosmochim Acta* 75(22):7117–7131.
7. Daëron M, Blamart D, Peral M, Affek HP (2016) Absolute isotopic abundance ratios and the accuracy of Δ_{47} measurements. *Chem Geol* 442:83–96.
8. Schauer AJ, Kelson J, Saenger C, Huntington KW (2016) Choice of ^{17}O correction affects clumped isotope (Δ_{47}) values of CO_2 measured with mass spectrometry. *Rapid Commun Mass Spectrom* 30(24):2607–2616.
9. Zaarur S, Affek HP, Brandon MT (2013) A revised calibration of the clumped isotope thermometer. *Earth Planet Sci Lett* 382:47–57.
10. Dennis KJ, Schrag DP (2010) Clumped isotope thermometry of carbonatites as an indicator of diagenetic alteration. *Geochim Cosmochim Acta* 74(14):4110–4122.
11. Tripati AK, et al. (2010) ^{13}C–^{18}O isotope signatures and “clumped isotope” thermometry in foraminifera and coccoliths. *Geochim Cosmochim Acta* 74(20):5697–5717.
12. Grauel A-L, et al. (2013) Calibration and application of the “clumped isotope” thermometer to foraminifera for high-resolution climate reconstructions. *Geochim Cosmochim Acta* 108:125–140.
13. Ghosh P, et al. (2006) ^{13}C–^{18}O bonds in carbonate minerals: A new kind of paleothermometer. *Geochim Cosmochim Acta* 70(6):1439–1456.
14. Carpenter WB (1850) On the Microscopic Structure of Nummulina, Orbitolites, and Orbitoides. *Q J Geol Soc* 6(1–2):21–39.
15. Beavington-Penney SJ, Wright VP, Racey A. (2006) The middle Eocene Seeb Formation of Oman: An investigation of acyclicity, stratigraphic completeness, and accumulation rates in shallow marine carbonate settings. *J Sediment Res* 76(10):1137–1161.
16. Gebhardt H, et al. (2013) Middle to late Eocene paleoenvironmental changes in a marine transgressive sequence from the northern Tethyan margin (Adelholzen, Germany). *Austrian J Earth Sci* 106(2):45–72.
17. Creech JB, Baker JA., Hollis CJ, Morgans HEG, Smith EGC (2010) Eocene sea temperatures for the mid-latitude southwest Pacific from Mg/Ca ratios in planktonic and benthic foraminifera. *Earth Planet Sci Lett* 299(3–4):483–495.
18. Pena LD (2005) Identification and removal of Mn-Mg-rich contaminant phases on foraminiferal tests: Implications for Mg/Ca past temperature reconstructions. *Geochemistry Geophys Geosystems* 6(9). doi:10.1029/2005GC000930.

19. Evans D, Müller W, Oron S, Renema W (2013) Eocene seasonality and seawater alkaline earth reconstruction using shallow-dwelling large benthic foraminifera. *Earth Planet Sci Lett* 381:104–115.
20. Renema W (2008) Habitat selective factors influencing the distribution of larger benthic foraminiferal assemblages over the Kepulauan Seribu. *Mar Micropaleontol* 68(3–4):286–298.
21. Renema W (2003) Larger foraminifera on reefs around Bali (Indonesia). *Zool. Verh. Leiden* 345:337–366.
22. Evans D, Brierley C, Raymo ME, Erez J, Müller W (2016) Planktic foraminifera shell chemistry response to seawater chemistry: Pliocene-Pleistocene seawater Mg/Ca, temperature and sea level change. *Earth Planet Sci Lett* 438:139–148.
23. Anand P, Elderfield H, Conte MH (2003) Calibration of Mg/Ca thermometry in planktonic foraminifera from a sediment trap time series. *Paleoceanography* 18(2). doi:10.1029/2002PA000846.
24. Locarnini R, et al. (2013) World Ocean Atlas 2013, Volume 1: Temperature. S. Levitus, Ed.; A. Mishonov, Technical Ed.; *NOAA Atlas NESDIS 73*, 40 pp.
25. Purton LMA, Brasier MD (1999) Giant protist Nummulites and its Eocene environment : Life span and habitat insights from $\delta^{18}O$ and $\delta^{13}C$ data from Nummulites and Venericardia, Hampshire basin, UK. *Geology* 27(8):711–714.
26. Gaillardet J, Dupré B, Louvat P, Allègre CJ (1999) Global silicate weathering and CO_2 consumption rates deduced from the chemistry of large rivers. *Chem Geol* 159(1–4):3–30.
27. Hall R (2002) Cenozoic geological and plate tectonic evolution of SE Asia and the SW Pacific : computer-based reconstructions, model and animations. *J Asian Earth Sci* 20:353–431.
28. Saraswati PK, Ramesh R, Navada SV (1993) Palaeogene isotopic temperatures of western India. *Lethaia* 26:89–98.
29. Anwar D, Choudhary A, Saraswati P (2013) Strontium isotope stratigraphy of the Naredi Formation, Kutch Basin , India. *Spec Publ Geol Soc India* 1:298–306.
30. Cotton LJ, Pearson PN (2011) Extinction of larger benthic foraminifera at the Eocene/Oligocene boundary. *Palaeogeogr Palaeoclimatol Palaeoecol* 311(3–4):281–296.
31. Nicholas CJ, et al. (2006) Stratigraphy and sedimentology of the Upper Cretaceous to Paleogene Kilwa Group, southern coastal Tanzania. *J African Earth Sci* 45(4–5):431–466.
32. King C (2016) A revised correlation of Tertiary rocks in the British Isles and adjacent areas of NW Europe, Eds. Gale AS, Barry TL (Geological Society of London Special Publications, London).
33. Plint AG (1983) Facies, environments and sedimentary cycles in the Middle Eocene, Bracklesham Formation of the Hampshire Basin: evidence for global sea-level changes? *Sedimentology* 30:625–653.
34. Bijl PK, et al. (2009) Early Palaeogene temperature evolution of the southwest Pacific Ocean. *Nature* 461(7265):776–9.
35. Frieling J, et al. (2014) Paleocene-Eocene warming and biotic response in the epicontinental West Siberian Sea. *Geology* 42(9):767–770.
36. Inglis GN, et al. (2015) Descent toward the Icehouse: Eocene sea surface cooling inferred from GDGT distributions. *Paleoceanography* 30(7):1000–1020.
37. Zachos JC, Dickens GR, Zeebe RE (2008) An early Cenozoic perspective on greenhouse warming and carbon-cycle dynamics. *Nature* 451(7176):279–83.

38. Evans D, Erez J, Oron S, Müller W (2015) Mg/Ca-temperature and seawater-test chemistry relationships in the shallow-dwelling large benthic foraminifera *Operculina ammonoides*. *Geochim Cosmochim Acta* 148:325–342.
39. Evans D, Müller W (2012) Deep time foraminifera Mg/Ca paleothermometry : Nonlinear correction for secular change in seawater Mg/Ca. *Paleoceanography* 27, PA4205, doi:10.1029/2012PA002315.
40. Rausch S, Böhm F, Bach W, Klügel A, Eisenhauer A (2013) Calcium carbonate veins in ocean crust record a threefold increase of seawater Mg/Ca in the past 30 million years. *Earth Planet Sci Lett* 362:215–224.
41. Coggon RM, Teagle D A H, Smith-Duque CE, Alt JC, Cooper MJ (2010) Reconstructing past seawater Mg/Ca and Sr/Ca from mid-ocean ridge flank calcium carbonate veins. *Science* 327:1114–7.
42. Horita J, Zimmermann H, Holland HD (2002) Chemical evolution of seawater during the Phanerozoic. *Geochim Cosmochim Acta* 66(21):3733–3756.
43. Gothmann AM, et al. (2015) Fossil corals as an archive of secular variations in seawater chemistry since the Mesozoic. *Geochim Cosmochim Acta* 160:188–208.
44. Dickson JAD (2002) Fossil echinoderms as monitor of the Mg/Ca ratio of Phanerozoic oceans. *Science* 298:1222–4.
45. Mucci A, Morse JW (1983) The incorporation of Mg^{2+} and Sr^{2+} into calcite overgrowths: influences of growth rate and solution composition. *Geochim Cosmochim Acta* 47:217–233.
46. De Choudens-Sanchez V, Gonzalez L A. (2009) Calcite and aragonite precipitation under controlled instantaneous supersaturation: Elucidating the role of $CaCO_3$ saturation state and Mg/Ca Ratio on calcium carbonate polymorphism. *J Sediment Res* 79(6):363–376.
47. Evans D, Müller W, Erez J Assessing foraminifera biomineralisation models through laser-ablation analysis of cultures under variable seawater chemistry. *Geochim Cosmochim Acta*. *In rev*.
48. Evans D, Wade BS, Henehan M, Erez J, Müller W (2016) Revisiting carbonate chemistry controls on planktic foraminifera Mg/Ca: Implications for sea surface temperature and hydrology shifts over the Paleocene-Eocene Thermal Maximum and Eocene-Oligocene transition. *Clim Past* 12(4):819–835.
49. Stanley SM, Hardie LA (1998) Secular oscillations in the carbonate mineralogy of reef-building and sediment-producing organisms driven by tectonically forced shifts in seawater chemistry. *Palaeogeogr Palaeoclimatol Palaeoecol* 144:3–19.
50. Wilkinson B, Algeo T (1989) Sedimentary carbonate record of calcium-magnesium cycling. *Am J Sci* 289:1158–1194.
51. Cramer BS, Miller KG, Barrett PJ, Wright JD (2011) Late Cretaceous–Neogene trends in deep ocean temperature and continental ice volume: Reconciling records of benthic foraminiferal geochemistry ($\delta^{18}O$ and Mg/Ca) with sea level history. *J Geophys Res* 116:1–23.
52. Farkaš J, et al. (2007) Calcium isotope record of Phanerozoic oceans: Implications for chemical evolution of seawater and its causative mechanisms. *Geochim Cosmochim Acta* 71:5117–5134.
53. Bijma J, Faber WW, Hemleben C (1990) Temperature and salinity limits for growth and survival of some planktonic foraminifers in laboratory cultures. *J Foraminifer Res* 20:95–116.

54. Uthicke S, Vogel N, Doyle J, Schmidt C, Humphrey C (2012) Interactive effects of climate change and eutrophication on the dinoflagellate-bearing benthic foraminifer Marginopora vertebralis. *Coral Reefs* 31(2):401–414.
55. Arieli RN, Almogi-Labin A, Abramovich S, Herut B (2011) The effect of thermal pollution on benthic foraminiferal assemblages in the Mediterranean shoreface adjacent to Hadera power plant (Israel). *Mar Pollut Bull* 62(5):1002–1012.
56. Schmidt C, Titelboim D, Brandt J, Herut B, Abramovich S (2016) Extremely heat tolerant photo- symbiosis in a shallow marine benthic foraminifera. *Sci Rep* 6(30930):1–9.
57. Schiebner C, Speijer RP, Marzouk AM (2005) Turnover of larger foraminifera during the Paleocene-Eocene Thermal Maximum and paleoclimatic control on the evolution of platform ecosystems. *Geology* 33(6):493–496.
58. Tyrrell T, Zeebe RE (2004) History of carbonate ion concentration over the last 100 million years. *Geochim Cosmochim Acta* 68(17):3521–3530.
59. Pearson PN, Foster GL, Wade BS (2009) Atmospheric carbon dioxide through the Eocene-Oligocene climate transition. *Nature* 461:1110–3.
60. Anagnostou E, et al. (2016) Changing atmospheric CO_2 concentration was the primary driver of early Cenozoic climate. *Nature* 533:380–384.
61. Hönisch B, et al. (2013) The influence of salinity on Mg/Ca in planktic foraminifers – Evidence from cultures, core-top sediments and complementary $\delta^{18}O$. *Geochim Cosmochim Acta* 121:196–213.
62. Hay WW, et al. (2006) Evaporites and the salinity of the ocean during the Phanerozoic: Implications for climate, ocean circulation and life. *Palaeogeogr Palaeoclimatol Palaeoecol* 240(1–2):3–46.
63. Taylor KWR, Huber M, Hollis CJ, Hernandez-Sanchez MT, Pancost RD (2013) Re-evaluating modern and Palaeogene GDGT distributions: Implications for SST reconstructions. *Glob Planet Change* 108:158–174.
64. Kim J-H, et al. (2010) New indices and calibrations derived from the distribution of crenarchaeal isoprenoid tetraether lipids: Implications for past sea surface temperature reconstructions. *Geochim Cosmochim Acta* 74(16):4639–4654.
65. Ho SL, Laepple T (2016) Flat meridional temperature gradient in the early Eocene in the subsurface rather than surface ocean. *Nat Geosci* 9:606–610.
66. Hollis CJ, et al. (2012) Early Paleogene temperature history of the Southwest Pacific Ocean: Reconciling proxies and models. *Earth Planet Sci Lett* 349–350:53–66.
67. Sluijs A., et al. (2011) Southern ocean warming, sea level and hydrological change during the Paleocene-Eocene thermal maximum. *Clim Past* 7(1):47–61.
68. Douglas PMJ, et al. (2014) Pronounced zonal heterogeneity in Eocene southern high-latitude sea surface temperatures. *Proc Natl Acad Sci* 111(18):6582–7.
69. Barke J, et al. (2012) Coeval Eocene blooms of the freshwater fern Azolla in and around Arctic and Nordic seas. *Palaeogeogr Palaeoclimatol Palaeoecol* 337:108–119.
70. Zeebe RE, Zachos JC (2007) Reversed deep-sea carbonate ion basin gradient during Paleocene-Eocene thermal maximum. *Paleoceanography* 22(3), PA3201, doi:10.1029/2006PA001395.
71. Lunt DJ, et al. (2010) CO_2-driven ocean circulation changes as an amplifier of Paleocene-Eocene thermal maximum hydrate destabilization. *Geology* 38(10):875–878.
72. Kiehl JT, Shields CA (2013) Sensitivity of the Palaeocene-Eocene Thermal Maximum climate to cloud properties. *Philos Trans A Math Phys Eng Sci* 371:20130093.

73. Huber M, Caballero R (2011) The early Eocene equable climate problem revisited. *Clim Past* 7(2):603–633.
74. Burgess CE, et al. (2008) Middle Eocene climate cyclicity in the southern Pacific: Implications for global ice volume. *Geology* 36(8):651.
75. Boscolo-Galazzo F, et al. (2014) The Middle Eocene Climatic Optimum (MECO): a Multi-Proxy Record of Paleoceanographic Changes in the South Atlantic (ODP Site 1263, Walvis Ridge). *Paleoceanography* 29:1143–1161.
76. Keating-Bitonti CR, Ivany LC, Affek HP, Douglas P, Samson SD (2011) Warm, not super-hot, temperatures in the early Eocene subtropics. *Geology* 39:771–774.
77. Liu Z, et al. (2009) Eocene-Oligocene Climate Transition. *Science* 323:1187–1190.
78. Pearson PN, et al. (2007) Stable warm tropical climate through the Eocene Epoch. *Geology* 35(3):211.
79. Sluijs A, et al. (2007) Environmental precursors to rapid light carbon injection at the Palaeocene/Eocene boundary. *Nature* 450:1218–1221.
80. Wade BS, et al. (2012) Multiproxy record of abrupt sea-surface cooling across the Eocene-Oligocene transition in the Gulf of Mexico. *Geology* 40(2):159–162.
81. Weller P, Stein R (2008) Paleogene biomarker records from the central Arctic Ocean (Integrated Ocean Drilling Program Expedition 302): Organic carbon sources, anoxia, and sea surface temperature. *Paleoceanography* 23(1), PA1S17, doi:10.1029/2007PA001472.
82. Bornemann A, et al. (2014) Persistent environmental change after the Paleocene-Eocene Thermal Maximum in the eastern North Atlantic. *Earth Planet Sci Lett* 394:70–81.
83. Hollis CJ, et al. (2015) The Paleocene–Eocene Thermal Maximum at DSDP Site 277, Campbell Plateau, southern Pacific Ocean. *Clim Past* 11(7):1009–1025.
84. Tripati AK (2004) Abrupt hydrographic changes in the equatorial Pacific and subtropical Atlantic from foraminiferal Mg/Ca indicate greenhouse origin for the thermal maximum at the Paleocene-Eocene Boundary. *Geochemistry Geophys Geosystems* 5(2), doi:10.1029/2003GC000631.
85. Penman DE, Zeebe RE, Thomas E, Zachos JC (2014) Rapid and sustained surface ocean acidification during the Paleocene-Eocene Thermal Maximum. *Paleoceanography* 29, doi:10.1002/2014PA002621.
86. Petersen SV, Schrag DP (2015) Antarctic ice growth before and after the Eocene-Oligocene transition: New estimates from clumped isotope paleothermometry. *Paleoceanography* 30(10):1305–1317.
87. Hines BR, et al. (2017) Reduction of oceanic temperature gradients in the early Eocene Southwest Pacific Ocean. *Palaeogeogr Palaeoclimatol Palaeoecol* 475:41–54.
88. Bijl PK, et al. (2013) Eocene cooling linked to early flow across the Tasmanian Gateway. *Proc Natl Acad Sci* 110(24):9645–9650.
89. Hollis CJ, et al. (2009) Tropical sea temperatures in the high-latitude South Pacific during the Eocene. *Geology* 37(2):99–102.
90. Tripati AK (2003) Tropical sea-surface temperature reconstruction for the early Paleogene using Mg/Ca ratios of planktonic foraminifera. *Paleoceanography* 18(4), doi:10.1029/2003PA000937.
91. Zachos JC, et al. (2003) A transient rise in tropical sea surface temperature during the Paleocene-Eocene thermal maximum. *Science* 302:1551–4.
92. Sagoo N, Valdes P, Flecker R, Gregoire LJ (2013) The Early Eocene equable climate problem: can perturbations of climate model parameters identify possible solutions?

Philos Trans R Soc A Math Phys Eng Sci 371(2001):20130123.

93. Van Hinsbergen DJJ, et al. (2015) A paleolatitude calculator for paleoclimate studies. *PLoS One* 10(6):1–21.
94. Dockery III DT (1996) Toward a revision of the generalized stratigraphic column of Mississippi. *Mississippi Geol* 17(1):2–8.
95. Saraswati PK, Sarkar U, Banerjee S (2012) Nummulites solitarius – Nummulites burdigalensis lineage in Kutch with remarks on the age of Naredia Formation. *Jour Geol Soc India* 79:476–482.
96. Erez J, Luz B (1983) Experimental paleotemperature equation for planktonic foraminifera. *Geochim Cosmochim Acta* 47:1025–1031.